Radiation Environment in the LHC Arc Sections During Run 2 and Future HL-LHC Operations

Kacper Biłko, Cristina Bahamonde Castro, Markus Brugger, Rubén García Alía, Yacine Kadi, Anton Lechner, Giuseppe Lerner, and Oliver Stein

***Abstract*— The Large Hadron Collider (LHC) at the European Organization for Nuclear Research (CERN) is the largest accelerator in the world, spanning a circumference of 26.7 km. During its operation, small fractions of the beams are being continuously lost. This leads to mixed-field radiation that might affect electronic equipment through both cumulative and single-event effects. This article considers the radiation environment during Run 2 (years 2015–2018) in the LHC arc sectors that constitute approximately 70% of the accelerator, housing a huge amount of electronics. There, the main magnets' configuration is periodic, and the main contributor to losses is the interaction of the beams with residual gas molecules, resulting in relatively low-radiation levels, as opposed to different parts of the LHC. However, as presented, there are locations where losses are no longer dominated by residual gas. In these locations, radiation levels are higher by up to more than two orders of magnitude and could, therefore, be problematic in terms of cumulative radiation effects on electronics. In this article, the dose measurements from beam loss monitors have been combined with the FLUKA simulation for the arc sectors in order to indirectly retrieve the residual gas densities and radiation profile under the magnet cryostats, at the equipment level, for the losses caused by residual gas. Estimations for the radiation levels in the arc sectors during the high-luminosity LHC era and potential implications for the electronics are discussed as well.**

***Index Terms*— Arc, beam loss monitors (BLMs), European Organization for Nuclear Research (CERN), FLUKA, high-energy hadron (HEH), HL-LHC, Large Hadron Collider (LHC), Monte Carlo methods, radiation effects, radiation monitors (RadMons), total ionizing dose (TID).**

I. Introduction

THE Large Hadron Collider (LHC) at the European Organization for Nuclear Research (CERN) is a circular collider, where two coplanar particle beams collide: one accelerated clockwise and the other anticlockwise [1]. It spans a total circumference of almost 27 km. Various beam loss mechanisms are present during its operation, leading to mixed field radiation. Through both single-event effects (SEEs) and cumulative effects, i.e., displacement damage (DD) and total ionizing dose (TID), it poses a threat to exposed electronics, hence to the accelerator performance [2].

During the first years of the LHC operation (Run 1, years 2009–2013), most of the radiation-to-electronics (R2E)-induced failures happened in the shielded areas near the interaction points (IP), where electronics were hardly radiation tolerant, or in the dispersion suppressor (DS) regions. Although electronics in these regions had been considered to be at risk and were partially tested, they were not qualified against radiation effects in a systematic and harmonized manner. Consequently, during the Long Shutdown 1 (LS1, years 2013–2015), in those areas, many mitigation activities, such as shielding or relocation, were performed [3]. Therefore, after LS1, in Run 2 (years 2015–2018), the relative importance of the arc regions increased. It implied the need for expansion of the radiation level monitoring and simulations from the shielded areas and DSs to the arcs, whose radiation environment was not studied in detail before.

A. General LHC Layout

The LHC is home to four fundamental CERN experiments. They are located at the centers of four insertion regions (IRs), where the two beams collide. In addition, the LHC contains four more IRs with the necessary accelerator elements, e.g., collimators, radio-frequency cavities, or beam dump systems. The schematic layout of the LHC is depicted in Fig. 1. DSs are placed at both sides of each IR. Their task is to interconnect the IR with the arc sections by adjusting beam optics parameters via magnet configuration. The LHC consists of smaller subsections that are called half-cells. An arc is defined as the part of the ring occupied by 46 regular half-cells [4] and is discussed in detail in Section I-D.

B. Sources of Radiation in the LHC

In the experimental IRs, collision debris, produced as a result of inelastic interactions, is lost downstream of the experiment. Accompanying secondary showers are the main source of radiation in the vicinity of the experiments. Provided that the operational conditions (e.g., energy) are the same, the losses are proportional to the luminosity of the experiment [5].

Manuscript received December 21, 2019; revised January 23, 2020; accepted January 24, 2020. Date of publication January 30, 2020; date of current version July 16, 2020.

The authors are with CERN, 1211 Geneva, Switzerland (e-mail: kacper.bilko@cern.ch).

Color versions of one or more of the figures in this article are available online at http://ieeexplore.ieee.org.

Digital Object Identifier 10.1109/TNS.2020.2970168

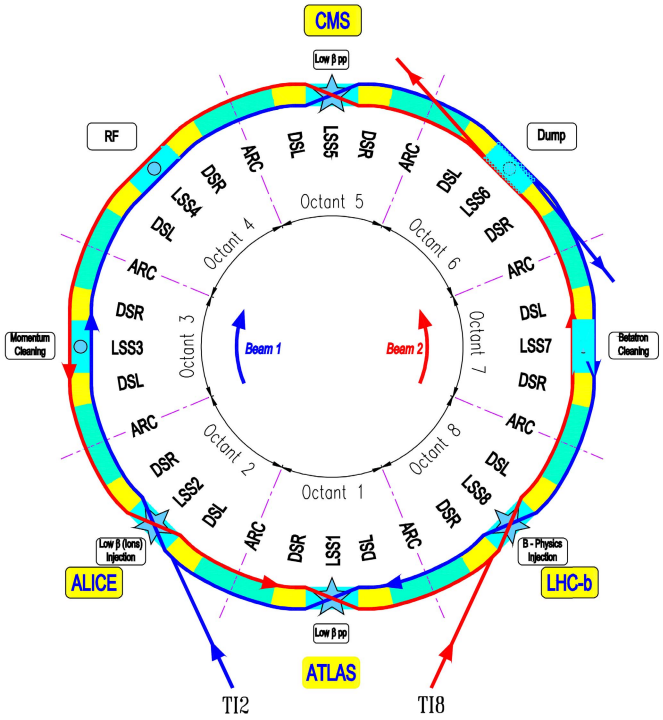

Fig. 1. Scheme of the LHC with the eight IRs, each containing a long, straight section (LSS: cyan areas) and two DSs (DSR and DSL: yellow areas). Arc sectors are marked with the green [4].

Collimator regions, located in IR 3 and IR 7, are used to intercept particles that do not have acceptable longitudinal or transverse oscillation amplitudes. Consequently, particles are stopped in the collimators that are designed to withstand high beam losses, hence high radiation levels.

In the LHC arc sectors, the main expected beam loss mechanism is the scattering of the beam on the residual gas inside the vacuum chamber. Scattered particles impact the beam screen (the innermost layer of the vacuum chamber). For the given beam energy, the radiation levels scale with the time-integrated beam intensity (absolute number of particles in the accelerator integrated over time) and the density of residual gas [5].

C. Radiation Monitoring in the LHC

To ensure undisturbed LHC operation, it is critical not only to qualify the equipment but also to monitor the radiation environment. The main quantities used at CERN to characterize it and, hence, evaluate the risk of damages and failures are as follows:

- TID—used to measure cumulative energy deposited through ionization that affects the lifetime of equipment;
- 1-MeV equivalent neutron fluence—applied to estimate the DD;
- equivalent high-energy hadron (HEH) fluence, defined as the time-integrated flux of hadrons above 20 MeV plus a weighted contribution of neutrons in the 0.2–20-MeV range [6], and thermal neutron fluence—both employed to assess the SEE probability.

Mainly two systems are used for active radiation monitoring in the LHC.

1) Beam Loss Monitors [7]: The beam loss monitor (BLM) system has been developed as a part of the LHC machine protection infrastructure. Its aim is to prevent damage to machine components and magnet quenches due to beam losses. It consists of more than 3600 ionization chambers, filled with nitrogen gas (volume of about 1.5 dm^3, at 1.1 bar [8]), distributed around the LHC in the critical locations.

Each chamber is a cylinder of approximately 50cm long, with parallel aluminum electrode plates, separated by 5 mm, working under 1.5 kV [9]. The charge collection time is below 0.1 ms.

The signal of the monitor is converted to pulses through a current-to-frequency converter. Pulses are counted over a period of 40 μs, and values are sent to ground electronics for further analysis [10]. Through the GEANT4 BLM simulation [11], values are converted to dose rate and logged in the CERN Accelerator Logging Service.

The first source of uncertainty of BLMs is the calibration process, which, in mixed field radiation, resulted in a difference up to 21% between GEANT4 BLM simulation and BLM measurement [11]. For radiation monitoring, the BLM signal has to be further processed in order to shift the signal to approximately 0 Gy/s once the beam is not present in the machine. In low-radiation areas, e.g., arc sections, neglecting further processing would lead to strong systematic TID overestimation by up to an order of magnitude. In the arc sections, especially in 2017 and 2018 when baseline dose rates were lower, the signal for some BLMs might have been close to the detection limit, leading to an increase of the relative uncertainty.

Although the fluences cannot be directly measured with BLMs, the FLUKA particle transport software [12], [13] enables us to perform simulations that can be later scaled with the BLM's TID measurements in order to retrieve fluences. For benchmarked regions, agreement between FLUKA simulations with the implemented BLMs and BLM measurements is better than 40% [14].

2) Radiation Monitors (RadMons): The RadMon system has been developed at CERN as a compact device that allows measuring the important quantities in terms of electronics damage [15]. It consists of RadFETs (p-channel MosFETs), which measure TID, silicon p-i-n diodes for the measurement of the 1-MeV equivalent neutron fluence, and SRAM memories for the HEH and thermal neutron fluences' evaluations. The accuracy of RadMon (version V6) measurements (fluences and doses) is below a factor 2 in complex and unknown radiation environments (e.g., LHC), while in calibration, it is 20% [16]. By the end of 2018, 392 RadMons were deployed in the LHC. Each RadMon unit, based purely on commercial electronics both for the sensors and data acquisition, processing, and transmission, has a TID lifetime of roughly 250 Gy [16].

D. LHC Arc Sectors

The arc section starts in the 12th half-cell of an IR and ends in the 12th half-cell of the next IR [4]. The nomenclature is the following: arc nm spans between the DSs of two neighboring IRs—IR n and IR m. Every two half-cells of

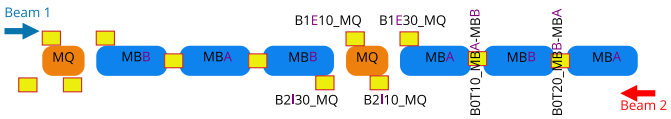

Fig. 2. Schematic representation of the LHC arc FODO cell with the BLMs locations (yellow rectangles). MQ denotes quadrupole magnet, whereas MB(B/A) denotes dipole ones. There are six different locations (BLM families) of BLMs with respect to the half-cell: four on the beams plane (B1_10, B1_30, B2_10, and B2_30), where B1s are located closer to the beam 1 and B2s closer to beam 2, and two on top of the interconnection between dipole magnets (B0T10 and B0T20). Magenta letters vary depending on the half-cell.

an arc section constitute a so-called FOcusing-DefOcusing (FODO) cell, where the main quadrupole (MQ) and main bending magnets (denoted as MBA and MBB) are periodically arranged. A schematic structure is illustrated in Fig. 2.

The installation pattern of the BLMs follows the periodic structure of FODO cells in the arcs—each half-cell contains six BLMs: four (two for each side) are located next to the quadrupole magnets (MQ) on the beam plane, and the remaining two are mounted on top of the pipe close to the interconnection of the dipole magnets (MB). A BLM family consists of all BLMs in LHC arcs that share the same functional position within the respective half-cell.

Moreover, each LHC arc cell contains additional magnets in order to correct nonlinear beam effects (e.g., chromaticity) and other electronic equipment, as follows:

- 60-A power converters with their controls (more than 750 units);
- quench protection system (QPS, almost 1500 units);
- cryogenics system (more than 500 units);
- beam instrumentation (360 units);
- vacuum control systems (almost 100 units).

As an example of a system sensitive to radiation in the LHC arc, the function generator control (FGC) is embedded in the computers directly installed in the 60-A corrector magnet power converters operating in the accelerator tunnel around the ring. A total of 758 units are distributed around the machine, performing digital processing and control of the power converter signals [17]–[19]. The FGC version initially installed in the accelerator (FGC2) experienced system-level soft SEEs, which resulted in the automatic rebooting of the system and loss of the beam in the accelerator. Such soft failures were experienced 15 times in total during the 2012-, 2015-, and 2016-LHC operation years (2013–2014 being the shutdown years) [20], which is a rate that, when extrapolated with future radiation levels and machine availability requirements, was incompatible with satisfactory operation. Therefore, an updated, radiation-tolerant version of the system (FGClite) was developed and qualified, and installed in the machine since 2017, having registered no failures due to radiation in two full years of operation (2017 and 2018). Indeed, the FGClite system is also fully compliant with the radiation lifetime and SEE rates tolerable for the high-luminosity LHC (HL-LHC, 2025-2035) operation [6].

The most critical equipment in terms of the TID lifetime is the 60-A power converter. It is estimated to withstand 25–50 Gy according to mixed-field tests performed prior to the LHC Run 1 (2010–2012).

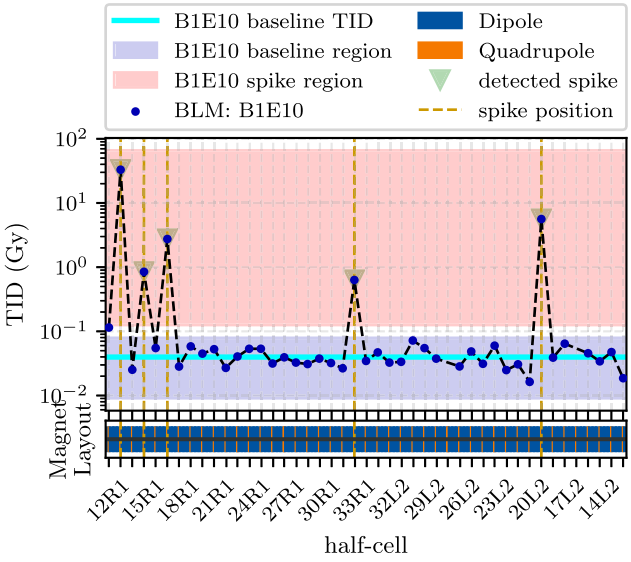

Fig. 3. TID (dose in N_2) measured during the 2018 p–p operation by the BLMs from B1E10 family (position illustrated in Fig. 2) in the arc sector 12. With few exceptions (spikes) majority of the BLMs measured similar dose level, i.e., baseline (estimated as an average TID measured within one BLM family excluding outliers).

II. Radiation Levels in the LHC Arc: Measurements and Simulations

A. General Arc Radiation Environment

We performed a detailed analysis of the radiation dose levels in the arc sections based on BLM data. As pointed out, the main beam loss mechanism in these regions is the interaction of the beam with residual gas molecules. The resulting cumulative radiation levels are proportional to both residual gas density and integrated beam intensity, defined as the time integral of the beam intensity during the LHC fills.

With the assumption that the residual gas density is constant over an arc section and all arc half-cells are identical (i.e., the attenuation profile for each half-cell is the same), it is expected that the measured loss levels within one BLM family are the same. The studies showed that the majority of the monitors reported similar doses (below 1 Gy for the entire Run 2) and time evolution. Based on their TIDs, a baseline level was defined, an example of which is depicted in Fig. 3. It is a typical dose level due to the losses caused by residual gas. Fig. 4 depicts the evolution of the baseline TID for six BLM families within one arc sector. Until mid-2017, nonlinear behavior can be observed with an approximately constant slope afterward. It is proof that baseline losses levels at the end of 2017 were the same as in 2018, suggesting achievement of the vacuum conditioned state. This trend was observed in all arc sectors.

However, among baseline BLMs, some localized anomalies (spikes) were detected, as can be observed in Fig. 3. For these spikes, the primary beam loss mechanism was no longer the beam-residual gas interaction. They can exceed the baseline by more than two orders of magnitude. In the case of

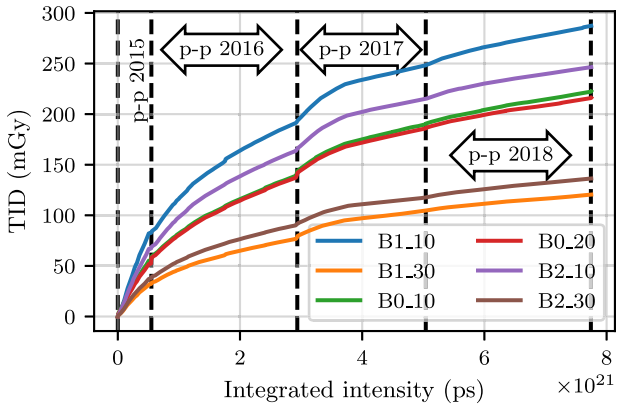

Fig. 4. Evolution of the baseline TID levels (dose in N_2) in the arc sector 12 over integrated beams intensity for top energy (protons with >5 TeV). Including integrated intensities for injection modes (protons with 450 GeV) has no impact on both the evolution and dose levels due to the low contribution of injection modes to total integrated intensity (less than 10% of total integrated beams intensity). Similar evolution trend was observed for all BLM families and all arc sectors—nonlinear evolution until mid-2017 and linearity afterward.

luminosity-driven spikes, the radiation levels scale with the integrated luminosity.

Most of the LHC uptime involves the proton–proton operation; hence, the primary focus is on these periods. With some significant exceptions, losses during ion operation in the LHC arc sectors are expected to be significantly lower due to reduced intensity. Annual BLM baseline levels for nominal LHC proton–proton operation (years 2016–2018) were in the 10–150-mGy range.

By design, one LHC beam consists of approximately 2800 bunches of $1.15 \cdot 10^{11}$ protons each (i.e., $3 \cdot 10^{14}$ circulating protons per beam). The revolution frequency is 11 245 Hz, corresponding, therefore, to a nominal beam current of 0.58 A [4]. Even if the beam intensity is reduced progressively due to collisions and other losses, an integrated beam intensity of $2.6 \cdot 10^{21}$ ps (for both beams) would be equivalent to $3 \cdot 10^{14}$ protons circulating in each beam during $4 \cdot 10^{6}$ s or 46 days. A typical LHC cycle (fill) lasts several hours and consists of injections, acceleration (from 450 GeV up to 6.5 TeV), and collisions of the beam. At the end of the fill, the beam is extracted from the machine. The evolution of the beam intensity during the typical fill is presented in Fig. 5.

The TID distribution normalized to the integrated intensity for both beams for BLMs that are installed near the quadrupoles (i.e., position 10) on the beam 1 side (according to Fig. 2) is shown in Fig. 6. Due to the normalization of annual integrated beam intensities, presented in Table I, the levels can be compared between different years. The normalized TID for all BLM families decreased over the years 2015–2017, but, in 2018, remained similar to 2017, suggesting the stabilization of the vacuum pressure [21].

B. Indirect Residual Gas Density Estimation

A FLUKA simulation of an LHC arc half-cell was performed in order to investigate the losses in the arc sectors in detail. The geometry is illustrated in Fig. 7. The assumptions

TABLE I

ANNUAL LHC INTEGRATED INTENSITIES FOR BOTH BEAMS FOR PROTON–PROTON OPERATION DURING RUN 2 [22]. THE INTEGRATED INTENSITY FOR EACH BEAM IS APPROXIMATELY THE HALF OF THE TOTAL INTEGRATED INTENSITY

Year	Total integrated intensity (10^{21} ps)	Integrated intensity for collision energy (10^{21} ps)
2015	0.716	0.505
2016	2.60	2.37
2017	2.51	2.10
2018	3.06	2.71

were that the only gas present in the beam pipe is hydrogen with a constant pressure profile and that the losses in both beams are the same. The real composition of the gases includes other gases as well (CO, CO_2, and CH_4); however, their contribution can be converted to hydrogen equivalent density [23]. The simulation provided TID values normalized to a fixed hydrogen equivalent gas density and to integrated intensity for each BLM family. Therefore, the comparison between the simulated and measured TID values during a period with known integrated beam intensity allows for an indirect retrieval of the respective gas density.

As illustrated in Fig. 8, in the years 2015–2017, the residual gas densities decreased in all arc sectors and remained the same in 2018. Furthermore, in 2018, the differences among arc sectors almost vanished. According to our regression, in 2018, the averaged, over all arc sectors, equivalent residual gas density was $(1.92 \pm 0.14) \cdot 10^{12} H_2$ molecules per m^3 (standard error of the mean). The obtained values cannot be directly compared with pressure measurements because the actual vacuum level is below the sensor detection limit [24].

The loss rate of the beam due to residual gas can be described with the following equation:

$$\frac{dN}{dt} = -\sigma d \rho f N = -\frac{1}{\tau} N \tag{1}$$

where N is the current beam intensity, σ is the cross section for the interaction of the beam with residual gas, d is the total length of arc sections, ρ is the number of gas molecules in a volume, f is the revolution frequency, and τ is the lifetime (time after the intensity decreases by a factor e) of the beam with respect to beam-residual gas interaction. Assuming $\rho = 2 \cdot 10^{12} H_2$ molecules per m^3, $\sigma = 94$ mb [25], $d = 8 \cdot 2.45$ km [4], and $f = 11\,245$ Hz [4], the corresponding lifetime would be $\tau = 2793$ days that is much above the minimum design limit, i.e., 100 h [4].

C. Radiation Profile Below an Arc Half-Cell

The FLUKA simulations provided the TID and fluence profiles both at BLM positions and below the magnet cryostat (60–80 cm below beam plane), the latter locations hosting the electronic racks potentially sensitive to radiation. The radiation levels need to be scaled with both residual gas density (presented in Fig. 8) and integrated intensity. Despite many assumptions, this approach enables us to evaluate radiation damage for arc electronics in the typical environment where losses are dominated by beam-residual gas interactions.

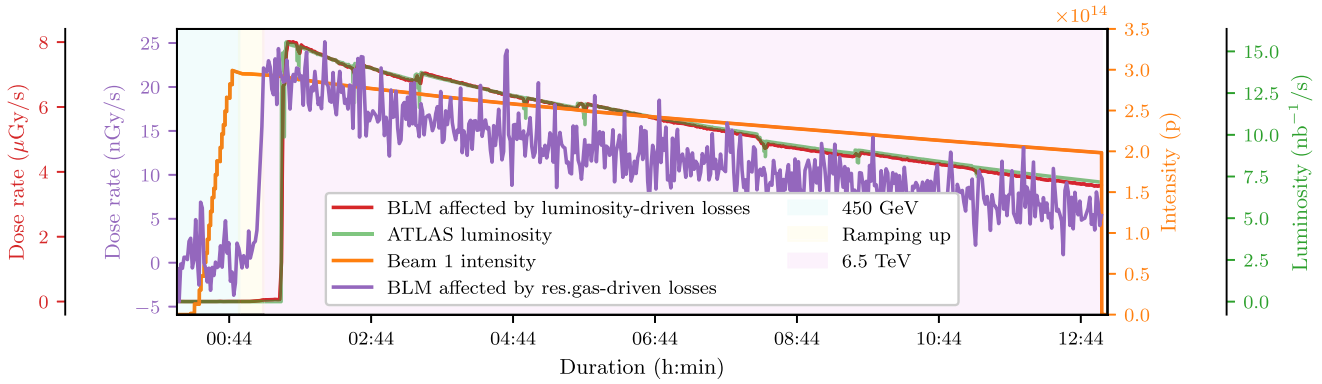

Fig. 5. Example of an LHC cycle (fill) with the signal from two BLMs: one affected by the losses caused by the luminosity production and one affected by losses dominated by residual gas. Beam intensity and luminosity of the ATLAS experiment has been plotted as a reference. Standard LHC fill consists of injection, acceleration, collisions, and, after several hours, the dump of the beams. For the BLM that is affected by luminosity-driven losses, the dose rate is strongly correlated with the luminosity of the causing experiment. However, for the BLM that is affected by the residual-gas scattering, losses begin once the collision energy (6.5 TeV) is achieved.

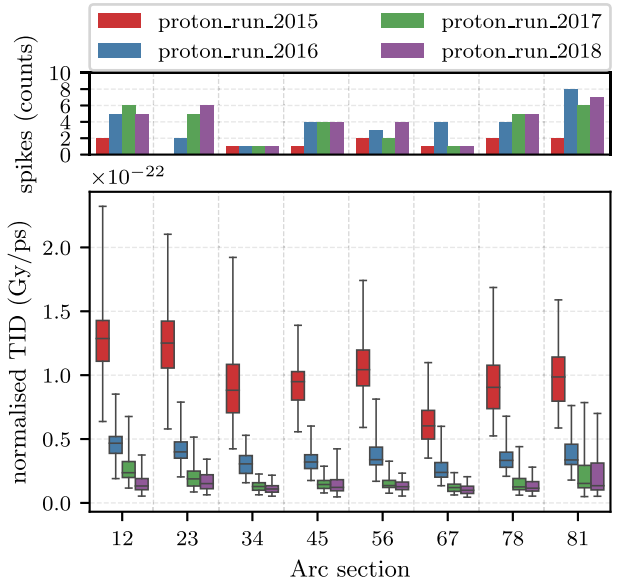

Fig. 6. Boxplot representation for normalized TID (dose in N_2 normalized to the annual integrated intensity for both beams) over the proton–proton operation during Run 2 for all arc sections. Only beam 1, position 10 BLM family considered. Box spans between the first and third quartiles. The median value is marked with a bar inside the box. Lower whisker represents the BLM with minimum TID. Upper one refers to the BLM with maximum TID, which is below spike threshold (defined as the $Q_3 + 3\text{IQR}$, where Q_3 is the third quartile and IQR is the interquartile range).

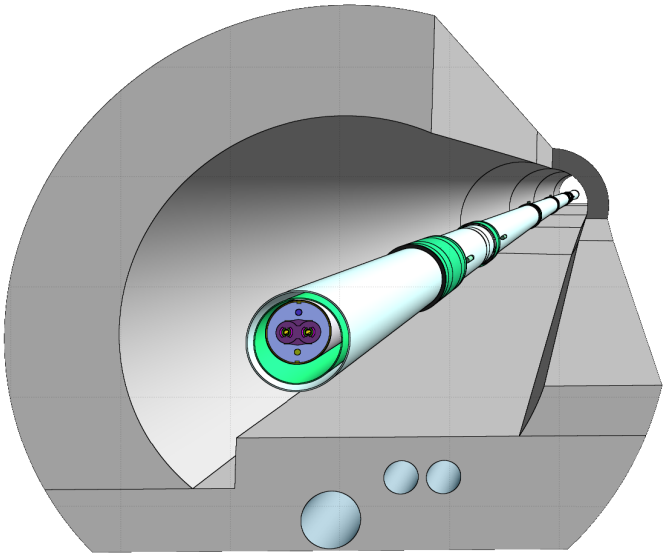

Fig. 7. Visualization of the FLUKA LHC arc geometry used in the simulation.

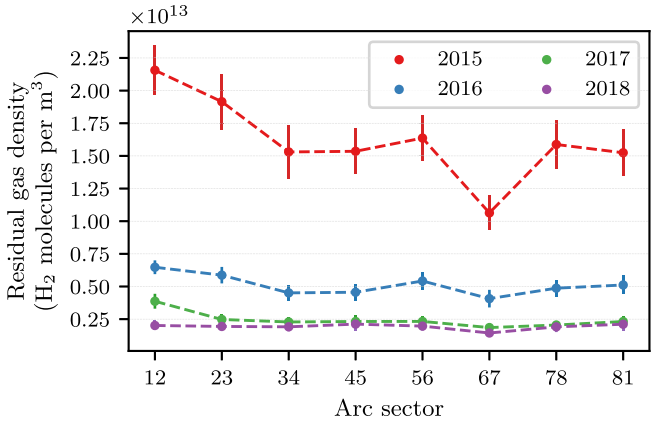

Fig. 8. Residual gas densities in all arc sections over Run 2 obtained via FLUKA simulations scaled with the baseline TID levels and integrated intensities.

The typical RadMon location in the arcs is below the cryostat, between the dipole and quadrupole magnet, in the so-called interconnect. They are installed in the 12th–21st half-cells. As shown in Fig. 9, in 2016, the averaged HEH fluence (excluding outliers) in the LHC arc sector 34, based on the RadMon measurements, was $5.0(1.1) \cdot 10^7$ cm^{-2} (uncertainty in terms of one standard deviation). The simulated value of the HEH fluence (blue trace), scaled with residual gas density and integrated intensity, at the approximated RadMon location, shown in Fig. 10) is $3.7 \cdot 10^7$ cm^{-2} with 17% uncertainty arising from residual gas estimation.

The agreement, comfortably within a factor 2, is a satisfactory benchmark of the described method. First, we obtained baseline TID levels measured using BLMs. Next, combining them with both the FLUKA simulation for BLMs and measured integrated intensities, we retrieved indirectly residual gas densities that were later used to scale FLUKA simulation

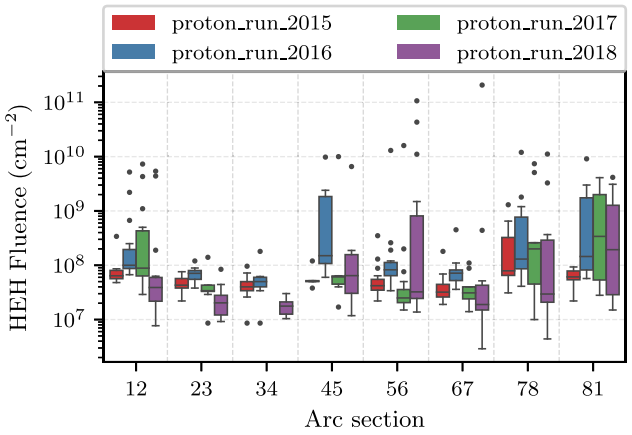

Fig. 9. Boxplot representation of the annual HEH fluences during the proton–proton operation in Run 2 measured by RadMons. Each box starts in the first quartile and ends in the third quartile. The upper (lower) whisker represents the last (first) data point that is within 1.5IQR distance from the third (first) quartile. The number of measurements for different arcs and years might vary. Data for the years 2015–2017 are taken from [26].

at the equipment level. One of the outputs was HEH fluence profile, which can be directly measured with RadMons. In 2016, in the arc sector 34, simulated fluence that we obtained was the same as an averaged measurement (within estimated uncertainties).

D. Critical Locations

As anticipated, in the arc sectors, many localized radiation anomalies (spikes) were detected. An example of spikes in the arc sector 12, during the 2018 proton–proton operation, is presented in Fig. 11. Sometimes, they exceed an arc baseline TID level by more than two orders of magnitude, therefore potentially having an impact on the nearby equipment. The most distinct spikes are caused by particles that have too large dispersion after passing by DS regions. In particular, they are observed in the starting odd half-cells (13, 15, and 17) of the arcs adjacent to high-luminosity experiments (IR 1 and IR 5).

Usually, spikes occur around quadrupole magnets due to local maxima of the β-function. Therefore, the doses visible in the quadrupole BLMs are higher than those in the dipole BLMs. An example of such behavior is illustrated in Fig. 12. The TID observed by the top BLMs, located less than 20 m away, is almost two orders of magnitude lower with respect to the highest TID measured by the quadrupole BLM. This spike is caused by the luminosity production in the ATLAS (IR 1) experiment. While majority of the arc spikes is caused by experiments (they scale with the luminosity), there were locations where the source of losses was different—an example is the 16th half-cell at the left-hand side of IP 2 where the spike was caused by the accidental air inflow [27] or the 15th half-cell at the right side of IP 8 where the spike was caused by the unidentified falling object (UFO) [28], [29].

E. Radiation Levels During Ion–Ion Operation

The LHC is operated with heavy ions as well, mainly with $^{208}Pb^{82+}$. However, ion operation lasts for a small fraction

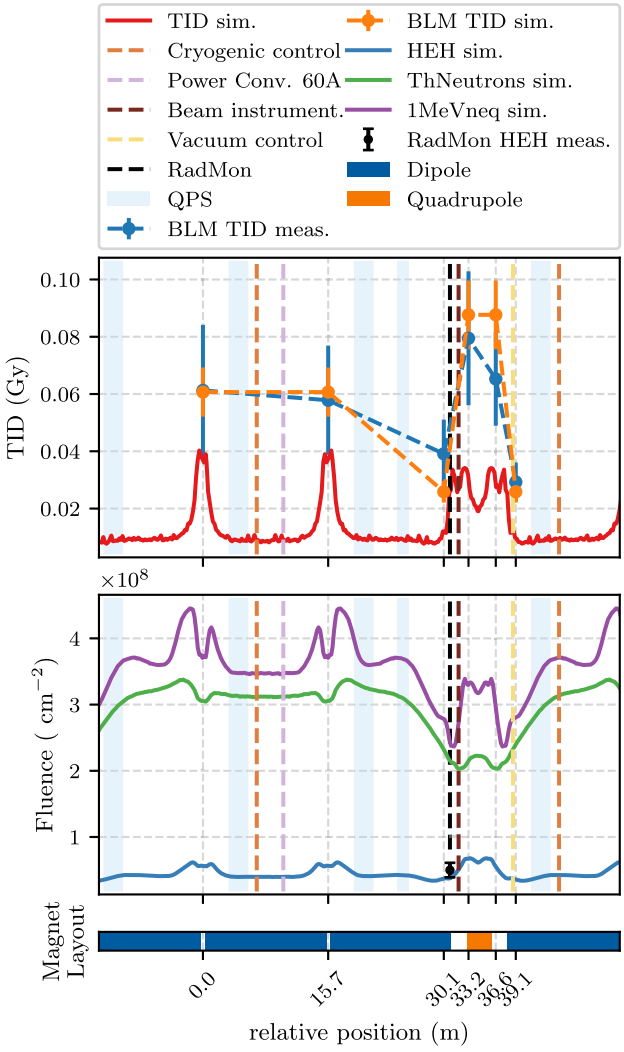

Fig. 10. Scaled TID (dose in air) and fluences' profiles below the magnet cryostats obtained via FLUKA in the typical half-cell of arc section 34 in 2016. Measurements and scaled simulation for BLMs (dose in N_2), with the estimated uncertainties, are depicted. Typical positions of electronic equipment are marked as well.

of the total LHC runtime, typically two to four weeks per year. During Run 2, 2015 and 2018 were the years that included a period of ion–ion physics in the LHC. In addition, the intensity is limited. In general, arc-losses and, consequently, the radiation levels caused by beam-residual gas interaction are negligible in comparison with the p–p operation. Nonetheless, in some locations, different loss mechanisms can be observed, resulting in a changed radiation profile. As an example, during the 2018 ion operation, positionwise symmetric spikes occurred in the 12th, 14th, and 16th half-cells, at both sides of IR 2. They are depicted in Fig. 13. Another region where significant losses during ion operation is momentum collimation region (IR 3—see Fig. 14). The most likely those ion spikes are caused by a beam loss mechanism typical for the ion operation—electromagnetic dissociation (EMD) [30] or bound-free pair production (BFPP) [31].

These relatively high radiation levels in the arc sections pose a threat to nearby electronics. The limited amount of space between the magnets and the electronic racks obstructs

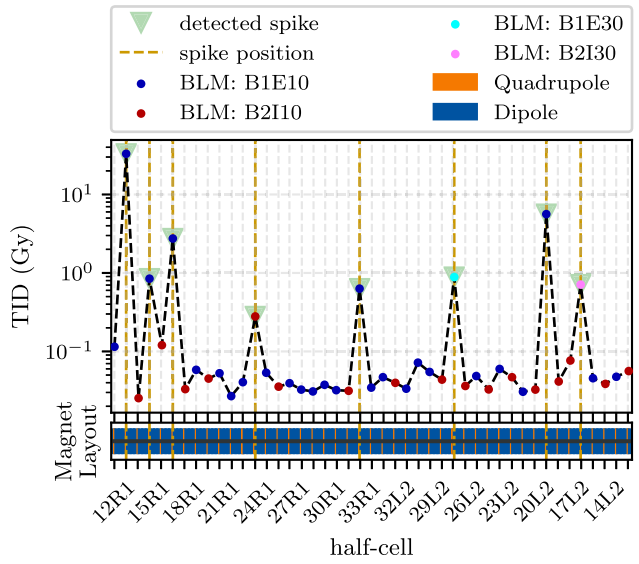

Fig. 11. Example of the spikes during the proton–proton operation in 2018 in the arc sector 12. Only side (quadrupole) BLMs have been considered, and the hottest one in each half-cell has been plotted (dose in N_2). The arc is approximately 2.4-km long.

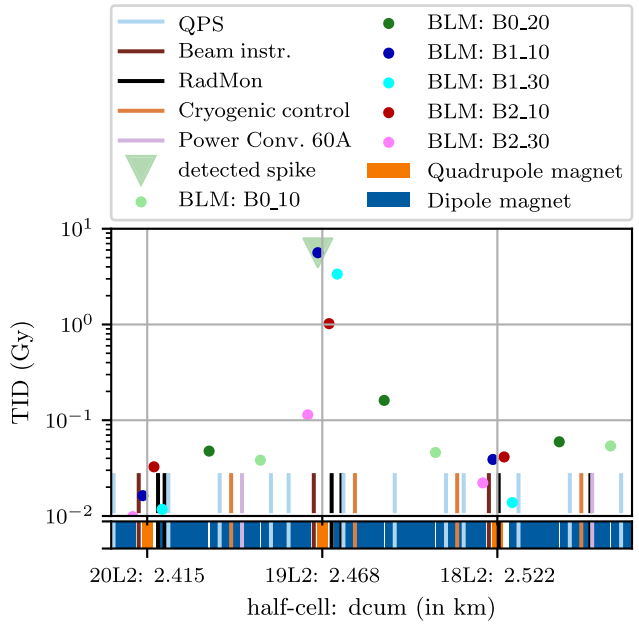

Fig. 12. TID measured by BLMs in the 18th, 19th, and 20th half-cells of the left-hand side of IR 2 (dose in N_2) during the proton–proton operation in 2018. The spike in 19L2 is marked with the triangle. Dcum is the longitudinal position in the LHC.

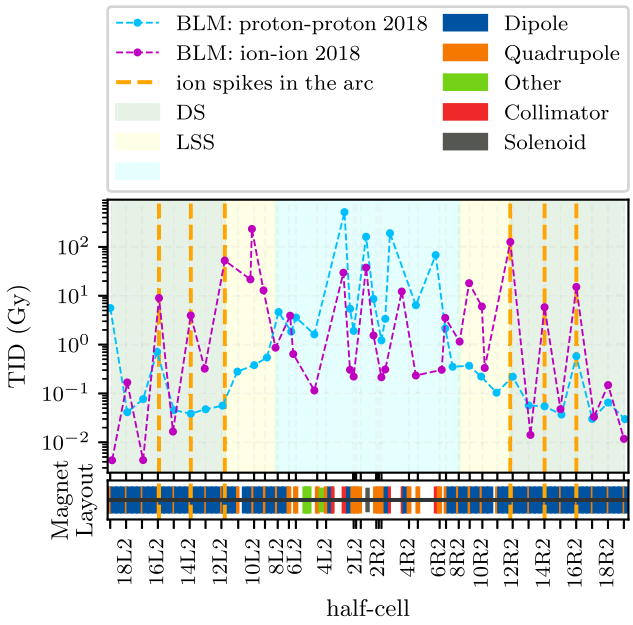

Fig. 13. TID (dose in N_2) levels measured around IP 2 (ALICE experiment) during the proton–proton and lead–lead operations in 2018. Only the maximum dose among side BLMs in each half is cell plotted.

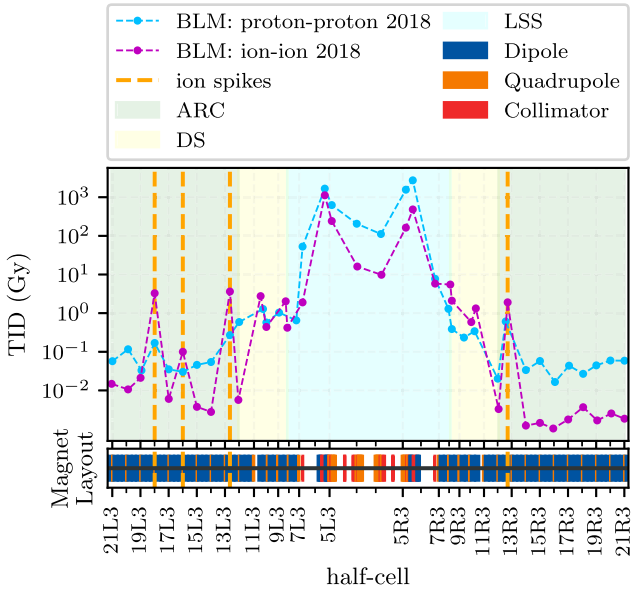

Fig. 14. TID (dose in N_2) levels measured around IP 3 (off-momentum cleaning) during the proton–proton and lead–lead operation in 2018. Only the maximum dose among side BLMs in each half is cell plotted.

the additional shielding installation; therefore, other mitigation actions, such as relocations, are advised.

F. Estimated Radiation Levels in the Arcs for the High-Luminosity LHC

It is possible to estimate both TID and fluences for the upgrade of the LHC, i.e., HL-LHC. It is predicted that during each year, HL-LHC operation will result in $8 \cdot 10^{21}$ ps of time-integrated beam intensity. Moreover, it is estimated that the residual gas density will, in the worst case, increase by a factor 4 with respect to the present operation due to the combined effect of synchrotron radiation and electron could [32]. Taking 2018 year and using mentioned scaling factors as a reference, we obtained the baseline TID and fluences' profiles (integrated over the full 12-year HL-LHC era) under the magnet cryostats. They are depicted in Fig. 15. It has to be pointed out that taking 2015 year as a reference would roughly result in one order of magnitude higher radiation levels.

As mentioned, the most vulnerable equipment in the arc sectors is the 60 A power converters, which can withstand 25 Gy.

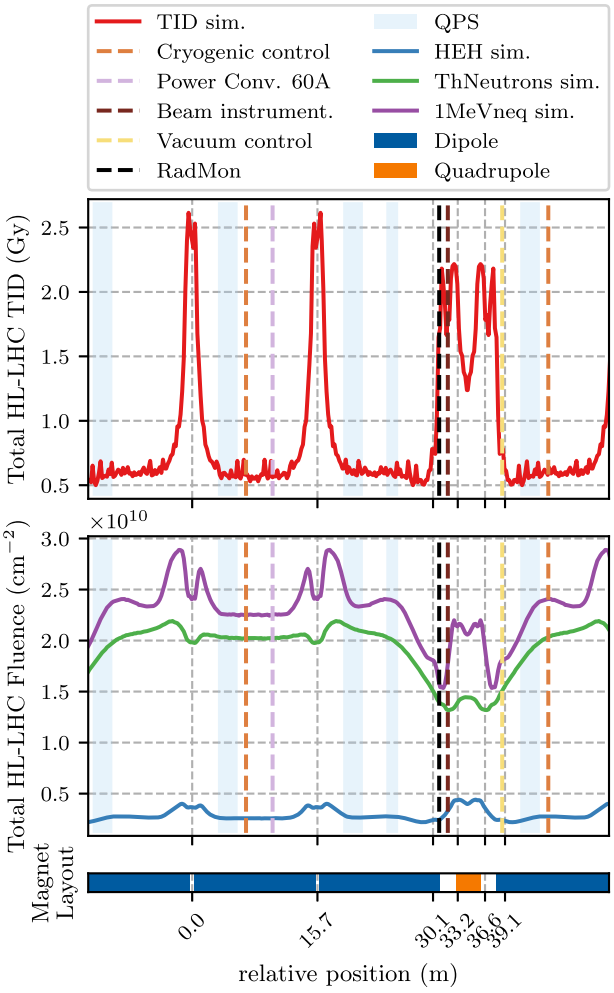

Fig. 15. Expected radiation environment (with 25% uncertainty, dose in air) below the cryostats for an arc half-cell integrated over the whole HL-LHC era. Typical positions of electronic equipment are marked as well.

The maximum TID that can be expected in the baseline half-cells at the equipment location is 2.5 Gy (with 25% uncertainty given in terms of one standard deviation). Therefore, this value does not suggest TID risk in the typical, baseline arc half-cells (under the mentioned assumptions).

However, it has to be kept in mind that some luminosity-driven spikes are present, especially close to DS regions. Assuming an overall HL-LHC luminosity of 4000 fb^{-1}, it is expected that maximum radiation levels at the equipment level in the 12th and 13th half-cells of high-luminosity experiments will achieve, respectively, few hundreds of Gy and 2 kGy. Such values pose tighter constraints to the COTS component selection and qualification for equipment located in these areas.

Moreover, SEEs are stochastic processes; thus, to evaluate the risk, the number of units has to be taken into account. Even though the radiation levels in the LHC arcs are not expected to affect the lifetime of commercial electronics for the full HL-LHC era, the HEH fluence values of roughly $4 \cdot 10^8$ cm^{-2}yr^{-1}, comparable to those present in LEO orbit in space, pose a serious SEE threat to the distributed COTS systems in the LHC arcs.

III. Conclusion

This article gives an account of the radiation environment in the LHC arc sectors during Run 2. With the novel approach that combined BLM measurements and FLUKA simulation of the arc half-cell, the residual gas densities were indirectly obtained. They decreased over the years of Run 2, remaining similar in both 2017 and 2018, implying, first, conditioning and, then, a stabilization of the LHC vacuum level. In addition, the radiation profile below the magnets where electronics are located has been retrieved. The scaled simulation of the HEH fluence is in agreement with the average baseline RadMon measurements. As opposed to other machine locations, such as the DS area, and according to baseline values measured and simulated for Run 2 operation, lifetime effects (TID and DD) on electronics are, in principle, not of concern for the HL-LHC equipment to be installed in the arc. However, there are several locations in which luminosity-driven spikes are observed, exceeding the baseline values by up to two orders of magnitude and, therefore, potentially compromising the lifetime of the nearby equipment; the presence of distributed systems in the machine, hosting tens of different active semiconductor references, and in the order of 10^3 units, still poses a significant threat and constraint with respect to SEE reliability. Therefore, it is critical to consider such SEE requirements in the system design and qualification, as well as to continuously monitor the radiation in that areas and carry out mitigation actions (e.g., relocation) if necessary.

References

[1] L. Evans and P. Bryant, "LHC machine," *J. Inst.*, vol. 3, no. 8, Aug. 2008, Art. no. S08001.
[2] R. Garcia Alia *et al.*, "LHC and HL-LHC: Present and future radiation environment in the high-luminosity collision points and RHA implications," *IEEE Trans. Nucl. Sci.*, vol. 65, no. 1, pp. 448–456, Jan. 2018.
[3] M. Brugger, "R2E and availability," in *Proc. LHC Perform. Workshop (Chamonix)*. Geneva, Switzerland: CERN, 2015, pp. 149–160. [Online]. Available: https://cds.cern.ch/record/2020930
[4] O. S. Bruning *et al.*, *LHC Design Report* (CERN Yellow Reports: Monographs). Geneva, Switzerland: CERN, 2004.
[5] O. Stein *et al.*, "A systematic analysis of the prompt dose distribution at the large hadron collider," in *Proc. 9th Int. Part. Accel. Conf. (IPAC)*, Vancouver, BC, Canada, no. 9. Geneva, Switzerland: JACoW, Jun. 2018, pp. 2036–2038, Paper WEPAF082.
[6] G. Apollinari *et al.*, *High-Luminosity Large Hadron Collider (HL-LHC): Technical Design Report V. 0.1* (CERN Yellow Reports: Monographs). Geneva, Switzerland: CERN, 2017. [Online]. Available: https://cds.cern.ch/record/2284929
[7] E. B. Holzer *et al.*, "Beam loss monitoring for LHC machine protection," *Phys. Procedia*, vol. 37, pp. 2055–2062, Dec. 2012.
[8] S. S. Gilardoni *et al.*, "Beam loss monitors comparison at the CERN proton synchrotron," in *Proc. 2th Int. Particle Accelerator Conf. (IPAC)*, San Sebastián, Spain, no. 2, Sep. 2011, pp. 1341–1343, Paper TUPC135.
[9] E. B. Holzer *et al.*, "Beam loss monitoring system for the LHC," in *Proc. IEEE Nucl. Sci. Symp. Conf. Rec.*, vol. 2, Oct. 2005, pp. 1052–1056.
[10] B. Dehning *et al.*, "The LHC beam loss measurement system," in *Proc. IEEE Part. Accel. Conf. (PAC)*, Jun. 2007, pp. 4192–4194.
[11] B. Dehning *et al.*, "LHC beam loss detector design: Simulation and measurements," in *Proc. IEEE Part. Accel. Conf. (PAC)*, Jun. 2007, pp. 4198–4200.
[12] T. BÖhlen *et al.*, "The FLUKA code: Developments and challenges for high energy and medical applications," *Nucl. Data Sheets*, vol. 120, pp. 211–214, Jun. 2014.
[13] A. Ferrari, P. Sala, A. Fasso, and J. Ranft, "FLUKA: A multi-particle transport code," *CERN Yellow Rep.*, vols. 10–2005, Jan. 2005, p. 405.
[14] A. Lechner *et al.*, "Validation of energy deposition simulations for proton and heavy ion losses in the CERN Large Hadron Collider," *Phys. Rev. A, Gen. Phys.*, vol. 22, Jul. 2019, Art. no. 071003.

[15] G. Spiezia *et al.*, "The LHC radiation monitoring system—RadMon," *Proc. Sci.*, vol. 143, pp. 1–12, Jan. 2011. [Online]. Available: https://pos.sissa.it/143/024
[16] G. Spiezia *et al.*, "A new RadMon version for the LHC and its injection lines," *IEEE Trans. Nucl. Sci.*, vol. 61, no. 6, pp. 3424–3431, Dec. 2014.
[17] B. Todd, A. Dinius, Q. King, and S. Uznanski, "Radiation tolerant power converter controls," *J. Inst.*, vol. 7, no. 11, Nov. 2012, Art. no. C11012.
[18] S. Uznanski, R. G. Alia, M. Brugger, C. Cangialosi, S. Danzeca, and B. Todd, "Qualification of electronic systems for radiation environments of high energy accelerator," in *Proc. 25th Int. Conf. 'Mixed Design Integr. Circuits Syst.' (MIXDES)*, Jun. 2018, pp. 34–38.
[19] S. Uznanski, B. Todd, A. Dinius, Q. King, and M. Brugger, "Radiation hardness assurance methodology of radiation tolerant power converter controls for large hadron collider," *IEEE Trans. Nucl. Sci.*, vol. 61, no. 6, pp. 3694–3700, Dec. 2014.
[20] S. Uznanski, B. Todd, A. Dinius, Q. King, and M. Brugger, "Systems overview: Power converter and their controls," in *Proc. 9th LHC Oper. Evian Workshop*. Geneva, Switzerland: CERN, submitted for publication. [Online]. Available: https://cds.cern.ch/record/2706427
[21] K. Bilko *et al.*, "Detailed analysis of the baseline dose levels and localized radiation spikes in the arc sections of the large hadron collider during run 2," in *Proc. 10th Int. Part. Accel. Conf. (IPAC)*, Melbourne, VIC, Australia, no. 10. Geneva, Switzerland: JACoW, Jun. 2019, pp. 4009–4012, paper THPRB083.
[22] O. Stein and K. Bilko, "Report on the prompt dose distribution along the LHC based on BLM data for proton-proton operation in run 2," CERN, Geneva, Switzerland, Tech. Rep. CERN-ACC-NOTE-2019-0040, Sep. 2019. [Online]. Available: https://cds.cern.ch/record/2692574
[23] A. Rossi, "Estimates of residual gas density in the LHC," in *Proc. LHC Workshop Experim. Conditions Beam Induced Detect. Backgrounds*. Geneva, Switzerland: CERN, 2009, pp. 26–29. [Online]. Available: https://cds.cern.ch/record/1184445
[24] V. Baglin, "The LHC vacuum system: Commissioning up to nominal luminosity," *Vacuum*, vol. 138, pp. 112–119, Apr. 2017.
[25] A. G. Mathewson and S. Zhang, "Beam-gas ionisation cross sections at 7.0 TeV," CERN, Geneva, Switzerland, Tech. Rep. LHC-VAC/AGM; Vacuum-Technical-Note-96-01, Jan. 1996. [Online]. Available: https://cds.cern.ch/record/1489148
[26] C. Martinella, "High energy hadrons fluence measurements in the LHC during 2015, 2016, and 2017 proton physics operations," CERN, Geneva, Switzerland, Tech. Rep. CERN-ACC-NOTE-2018-0088, Dec. 2018. [Online]. Available: http://cds.cern.ch/record/2652458
[27] J. Jimenez *et al.*, "Observations, analysis and mitigation of recurrent LHC beam dumps caused by fast losses in arc half-cell 16L2," in *Proc. 9th Int. Part. Accel. Conf. (IPAC)*, Vancouver, BC, Canada, no. 9. Geneva, Switzerland: JACoW, Jun. 2018, pp. 228–231, Paper MOPMF053.
[28] D. Mirarchi *et al.*, "LHC aperture and ULO restrictions: Are they a possible limitation in 2016?" in *Proc. 6th Evian Workshop LHC Beam Oper.* Geneva, Switzerland: CERN, 2016, pp. 87–94.
[29] B. Lindstrom *et al.*, "Results of UFO dynamics studies with beam in the LHC," in *Proc. 9th Int. Part. Accel. Conf. (IPAC)*, Vancouver, BC, Canada, no. 9. Geneva, Switzerland: JACoW, Jun. 2018, pp. 2914–2917, Paper THYGBD2.
[30] R. Bruce, "Beam loss mechanisms in relativistic heavy-ion colliders," Ph.D. dissertation, MAX-lab, Lund, Sweden, 2009. [Online]. Available: https://cds.cern.ch/record/1246025
[31] C. B. Castro *et al.*, "Power deposition in LHC magnets due to bound-free pair production in the experimental insertions," in *Proc. Int. Part. Accel. Conf. (IPAC)*, Busan, South Korea, no. 7. Geneva, Switzerland: JACoW, Jun. 2016, pp. 1418–1421, Paper TUPMW006.
[32] G. Iadarola *et al.*, "Electron cloud and heat loads in run 2," in *Proc. 9th LHC Oper. Evian Workshop*. Geneva, Switzerland: CERN, submitted for publication. [Online]. Available: https://cds.cern.ch/record/2706427